

LiFCal: Online Light Field Camera Calibration via Bundle Adjustment

Aymeric Fleith^{1,2}, Doaa Ahmed², Daniel Cremers¹, and Niclas Zeller²

¹ Technical University of Munich, Munich, Germany
 {aymeric.fleith, cremers}@tum.de

² Karlsruhe University of Applied Sciences, Karlsruhe, Germany
 {doaa.ahmed, niclas.zeller}@h-ka.de

Abstract. We propose LiFCal, a novel geometric online calibration pipeline for MLA-based light field cameras. LiFCal accurately determines model parameters from a moving camera sequence without precise calibration targets, integrating arbitrary metric scaling constraints. It optimizes intrinsic parameters of the light field camera model, the 3D coordinates of a sparse set of scene points and camera poses in a single bundle adjustment defined directly on micro image points.

We show that LiFCal can reliably and repeatably calibrate a focused plenoptic camera using different input sequences, providing intrinsic camera parameters extremely close to state-of-the-art methods, while offering two main advantages: it can be applied in a target-free scene, and it is implemented online in a complete and continuous pipeline.

Furthermore, we demonstrate the quality of the obtained camera parameters in downstream tasks like depth estimation and SLAM.

Webpage: <https://lifcal.github.io/>.

Keywords: Plenoptic camera · Light field · Micro lens array · Online calibration · Target-free calibration · Plenoptic bundle adjustment · Metric depth estimation

1 Introduction

Visual odometry (VO) and simultaneous localization and mapping (SLAM) are expanding in fields like virtual reality, augmented reality, autonomous driving, using mainly monocular [11,12], stereo [37] or RGB-D cameras [28]. Monocular cameras cannot determine scene scale without prior knowledge, stereo cameras are less stable in calibration, and RGB-D cameras need active scene illumination.

The concept of light field cameras has been around for many years [19,24] and its value in depth estimation [38], super resolution [39], VO and SLAM [48] is clear. What’s more, it has a very large depth of field. Their appeal has grown with advancements in GPU processing and market availability, but cumbersome calibration has limited their mainstream adoption. As camera configurations change, target-free online calibration is essential for accurate data, *e.g.* accurate 3D reconstruction. We address these shortcomings by introducing LiFCal, a new

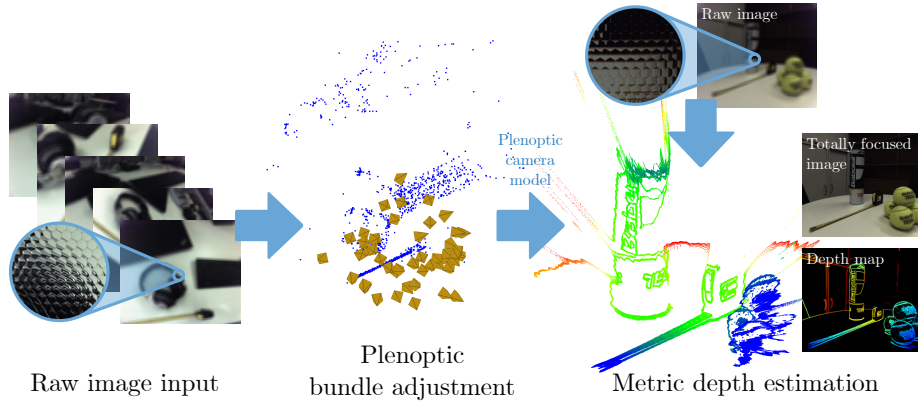


Fig. 1. Process overview: Raw images undergo camera calibration via plenoptic bundle adjustment. This yields a metric camera model used to compute a totally focused image and depth map from new raw images, enabling accurate metric depth measurement.

online calibration pipeline for micro lens array (MLA)-based light field cameras, called plenoptic cameras in the sequel. To our knowledge, this is the first target-free calibration method for a complete plenoptic camera model, specifically for VO or SLAM. LiFCal offers the following key contributions:

- An online calibration pipeline that accurately determines all intrinsic parameters of a plenoptic camera in scenes without a calibration target.
- A bundle adjustment formulation minimizing reprojection errors directly on micro image coordinates of a plenoptic camera and integrating arbitrary metric scaling constraints, acting as a complete structure from motion (SfM) pipeline for MLA-based plenoptic cameras.
- The integration of the plenoptic camera model into a micro-image-based depth estimation approach, providing undistorted metric depth maps and synthesized intensity images following the process described in Fig. 1.

We evaluate our pipeline’s performance against state-of-the-art target-based plenoptic camera calibration on a public dataset [49] and our own recordings. We demonstrate that our results closely match the reference calibration [42] with good precision and repeatability, enabling reliable metric point cloud generation.

The paper is organized as follows. Sec. 2 presents related work on plenoptic camera and online camera calibration. Sec. 3 introduces the LiFCal calibration method, covering the geometric model, the calibration pipeline, the initialization, and the plenoptic bundle adjustment. Sec. 4 provides an extensive evaluation of the method and demonstrates the camera model’s usability in tasks such as metric depth estimation and SLAM. Sec. 5 summarizes and concludes the work.

2 Related Work

Our method enables online calibration of plenoptic cameras. This section covers both calibration for these cameras and online calibration for other cameras.

2.1 Plenoptic Camera Calibration

Several publications deal with the calibration of plenoptic cameras. They can be divided in two types: unfocused plenoptic cameras (or plenoptic camera 1.0) and focused plenoptic cameras (or plenoptic camera 2.0).

Unfocused Plenoptic Cameras. Unfocused plenoptic cameras were studied more closely in [1,30]. The main lens is focused on the MLA, which is itself focused to infinity. The sensor plane is placed at the focal plane of the MLA.

A first method for correcting main lens aberrations on 4D light field data is introduced in [29]. [8] presents a full MLA calibration pipeline for Lytro cameras. The first complete mathematical model for general unfocused plenoptic cameras is introduced in [9], including fifteen parameters and based on angle detection in sub-apertures images. It is refined by [51] to represent physical camera parameters. A hybrid calibration approach by [10], calibrates sub-aperture images using geometric constraints of the main and micro lenses. [20] uses a multi-view light field for calibration.

To improve feature detection in low-resolution micro images, [3] uses line features from micro images, instead of the feature points used so far, and [31,50] introduce a model using plenoptic discs.

Focused Plenoptic Cameras. For improved resolution, [26,27] explore the trade-off between spatial and angular information in light field data, leading to a focused plenoptic camera. The MLA is placed either in front or behind the image plane. Furthermore, the micro lenses are focused at the main lens’s image plane rather than infinity, enhancing spatial resolution at the expense of angular precision.

The first calibration method for focused plenoptic cameras is introduced in [21], using a fifteen-parameter model for a Raytrix camera and accounting for lateral image distortion. It is further refined in [18] with automatic calibration and an improved main lens distortion model, using a flat reference target.

In [43], three new models use the light field to relate object distance and virtual depth. Virtual depth calibration is added in [46]. [41] addresses lateral distortion after projecting virtual image points. The calibration approach [47] estimates all intrinsic parameters, 3D object points, and camera poses in one task, reducing parameters to five but requiring a specific 3D target.

A calibration algorithm for multi-focus plenoptic cameras using only raw images is presented in [22,23] by introducing a new Blur Aware Plenoptic feature.

[14] calibrates the sub-aperture views considering images as a set of pinhole views. This approach is extended in [13] for use without a reference pattern.

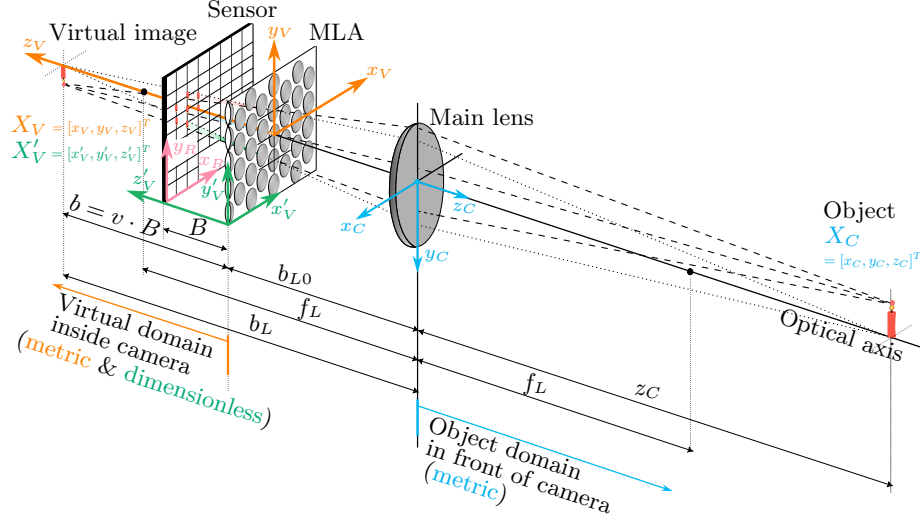


Fig. 2. Focused plenoptic camera in Galilean mode. Parameter f_L is the main lens focal length, b_{L0} the distance between main lens and MLA, B the distance between MLA and sensor, b the distance between MLA and virtual image, b_L the distance between main lens and virtual image and z_C the distance between real object and main lens. The virtual image created by the main lens is a mirror image of the real scene.

2.2 Online Camera Calibration

Camera calibration typically requires a target. Online methods, however, determine intrinsic and extrinsic parameters without needing prior scene information.

Early target-free calibration methods [6,33] relied on scene assumptions and known environment structures. Newer geometric approaches enable online calibration of monocular cameras in arbitrary scenes. In [36], the camera is calibrated while reconstructing the scene, determining parameters for each view. [25] uses a convolutional neural network to estimate camera parameters from a panorama. [15] presents a self-supervised method using unconstrained image sequences.

Auto calibration extends to other camera types. [40] calibrates an RGB-D camera using sparse 3D reconstruction with SfM or SLAM. [34] allows online depth calibration for an RGB-D camera using a visual SLAM system without manual intervention. [35] introduces an online calibration system for stereo cameras, optimizing intrinsic and extrinsic parameters through bundle adjustment, starting with 3D scene reconstruction and trajectory estimation to optimize the parameters using a nonlinear solver. [7] proposes a target-free calibration for a stereo camera-GNSS/IMU system, beginning with parameter initialization via reconstruction, followed by refinement with a solver.

3 LiFCal Calibration Method

This section presents the plenoptic camera model (Sec. 3.1) used for calibration and metric depth estimation, as background, inspired by [47], and the complete

proposed calibration pipeline (Sec. 3.2), including initial calibration and plenoptic bundle adjustment. The proposed LiFCal method does not require prior scene knowledge or targets, enabling better conditioning by using points with greater depth and spacing, overcoming limitations of simpler targets like checkerboards.

3.1 Plenoptic Camera Model

Using a MLA between main lens and sensor (see Fig. 2), a plenoptic camera captures a 4D light field in a single image. The plenoptic camera model used in LiFCal is inspired by [47] and employs a thin lens model for the main lens and a pinhole model for each micro lens. Lens distortion is defined directly on MLA and raw image coordinates. While the camera model is introduced based on a focused plenoptic camera, it generally also holds for an unfocused plenoptic camera. However, no manufacturers currently produce unfocused plenoptic cameras.

In the Galilean mode (see [26] for the difference between Keplerian and Galilean modes), the main lens projects a 3D object space into a 3D virtual image space (see Fig. 2). A 3D point in object space is defined by its metric camera coordinates $X_C = [x_C, y_C, z_C]^T$ or homogeneous coordinates $\bar{X}_C = [x_C, y_C, z_C, 1]^T$.

Using the thin lens model, an object point X_C can be projected into the virtual image space with coordinates $X_V = [x_V, y_V, z_V]^T$ (or homogeneous coordinates $\bar{X}_V = [x_V, y_V, z_V, 1]^T$). The virtual image space, with its origin at the intersection of the main lens' optical axis and the MLA, is a mirrored coordinate system, meaning that its axes are all in the opposite direction compared to the camera frame. Hence, the projection from X_C to X_V is defined as follows:

$$\lambda \cdot \bar{X}_V = K \cdot \bar{X}_C \quad \Leftrightarrow \quad \lambda \cdot \begin{bmatrix} x_V \\ y_V \\ z_V \\ 1 \end{bmatrix} = \begin{bmatrix} b_L & 0 & 0 & 0 \\ 0 & b_L & 0 & 0 \\ 0 & 0 & b & 0 \\ 0 & 0 & 1 & 0 \end{bmatrix} \cdot \begin{bmatrix} x_C \\ y_C \\ z_C \\ 1 \end{bmatrix}. \quad (1)$$

The parameters b_L and b depend on the object point distance z_C . The relation between b_L , b and z_C is expressed based on the thin lens equation in Eq. (2).

$$b_L = \left(\frac{1}{f_L} - \frac{1}{z_C} \right)^{-1} = b + b_{L0} \quad (2)$$

A point in metric coordinates X_V in the virtual image is converted to dimensionless coordinates $X'_V = [x'_V, y'_V, z'_V]^T$. x'_V and y'_V are defined in pixels (Eq. (3)), while z'_V is defined by the so called virtual depth v (Eq. (4)), introduced in [32] to generate depth maps from plenoptic images without metric calibration [44]. In Eq. (3), s_x and s_y represent pixel size and $C_L = [c_x, c_y]^T$ is the principal point of the main lens. While pixel dimensions are not essential, they provide a metric reference for the parameters.

$$x'_V = x_V \cdot s_x^{-1} + c_x, \quad y'_V = y_V \cdot s_y^{-1} + c_y \quad (3)$$

$$v = \frac{b}{B} = \frac{b_L - b_{L0}}{B} \Rightarrow b_L = v \cdot B + b_{L0} \quad (4)$$

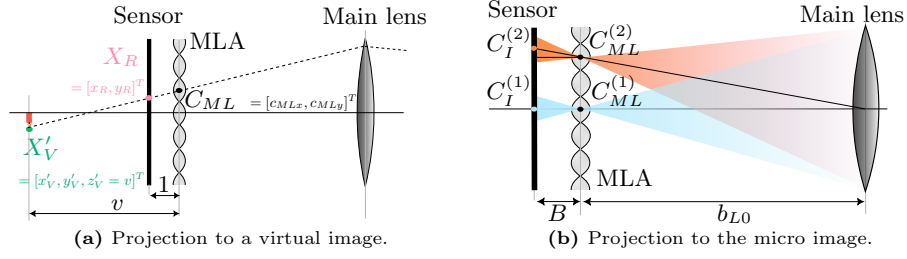


Fig. 3. Projection modeling inside the plenoptic camera. (a) Projection of a virtual image point $X'_V = [x'_V, y'_V, z'_V = v]^T$ to a raw image point $X_R = [x_R, y_R]^T$ through the micro lens center $C_{ML} = [c_{MLx}, c_{MLy}]^T$. The virtual image point is given in dimensionless coordinates, *i.e.* image distance $b = v \cdot B$ is normalized by the distance B . (b) Projection from the micro lens centers C_{ML} to the micro image centers C_I .

A point X'_V in the virtual image can be projected to multiple points $X_R = [x_R, y_R]^T$ in the raw image as defined in Eq. (5) (see Fig. 3a for reference), *i.e.* observations of the same virtual image point in multiple micro images. Here, $C_{ML} = [c_{MLx}, c_{MLy}]^T$ is the center of the associated micro lens.

$$x_R = (x'_V - c_{MLx}) \cdot v^{-1} + c_{MLx}, \quad y_R = (y'_V - c_{MLy}) \cdot v^{-1} + c_{MLy} \quad (5)$$

In reality, micro image centers $C_I = [c_{Ix}, c_{Iy}]^T$ are not directly aligned with micro lens centers C_{ML} (see Fig. 3b). In Eq. (5), the micro lenses centers C_{ML} are derived from micro image centers C_I using Eq. (6). The centers C_I can be determined beforehand using a white image recorded with the plenoptic camera.

$$C_{ML} = \begin{bmatrix} c_{MLx} \\ c_{MLy} \\ b_{L0} \end{bmatrix} := C_I \cdot \frac{b_{L0}}{b_{L0} + B} = \begin{bmatrix} c_{Ix} \\ c_{Iy} \\ b_{L0} + B \end{bmatrix} \cdot \frac{b_{L0}}{b_{L0} + B} \quad (6)$$

The presented camera model projects an object point X_C to multiple points X_R on the recorded raw image, *i.e.* into multiple micro images. To account for position imperfections due to lens distortion and sensor misalignment, a lens distortion model is added. Unlike other plenoptic camera models, distortion is applied directly to the recorded raw image, *i.e.* on the micro image coordinates and micro lens centers. This way, the distortion model can be integrated directly into downstream tasks like image synthesis and depth estimation (see Sec. 4.2). Therefore, a complex model for virtual depth distortion [18], which in general cannot be inverted in closed form, is omitted. The model employs radial symmetric and tangential distortion based on [4] (see supplementary material for details), though it can be substituted with any other distortion model.

While the micro image centers can be obtained beforehand, in addition to the distortion parameters, the model leaves five unknown parameters to be determined and optimized for camera calibration: focal length f_L ; main lens principal point $C_L = [c_x, c_y]^T$ in pixels; distance B between the MLA and the sensor; distance b_{L0} between the main lens and the MLA.

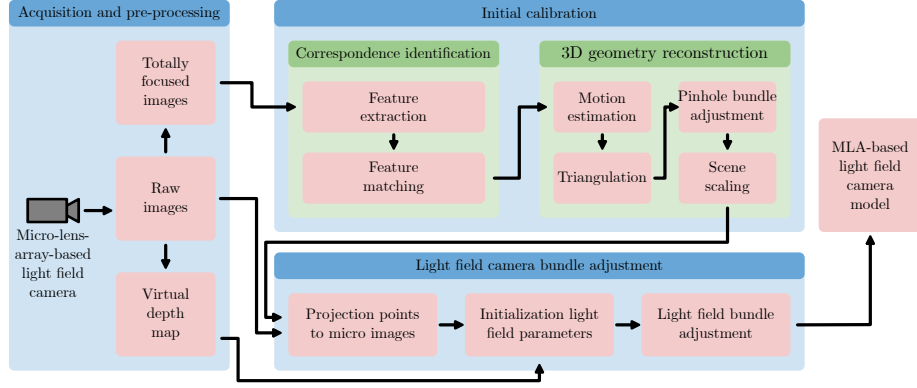


Fig. 4. Flowchart of the online calibration algorithm for the focused plenoptic camera. Images are acquired from the camera and are first used to initialize the parameters. Next, a complete bundle adjustment for the plenoptic camera model is performed.

3.2 Calibration Pipeline

Unlike the eight-point algorithm, solving the two view geometry problem for a monocular camera, a closed-form solution cannot be built for the raw images of a plenoptic camera. Each pair of micro images provides a different fundamental matrix. Several point correspondences would be required per micro image pair, which is not possible because of their small size.

The proposed pipeline, shown in Fig. 4, starts with acquiring raw data from the plenoptic camera (Fig. 1). From the estimated virtual depth v and the raw image, we generate the so-called totally focused image and the virtual depth map [44]. The totally focused image is only for feature detection to initiate bundle adjustment. Similarly, depth maps and raw images serve only for initialization, where precise values are not crucial, as parameters are optimized based on micro image coordinates X_R . The initialization uses a pinhole camera model to get a first estimate of all camera poses, intrinsic parameters of the pinhole model and 3D point coordinates. The plenoptic model is then used to determine the exact intrinsic and extrinsic camera parameters and a sparse scene reconstruction in a plenoptic bundle adjustment formulation.

Initial Calibration. For initialization, the plenoptic camera is modeled as a pinhole camera, estimating approximate values of all camera poses, intrinsic parameters of the pinhole model and 3D point coordinates [47]. SIFT features are extracted and matched from totally focused images, with outliers removed via RANSAC [16]. Assuming a static scene, initial camera poses $\xi \in \mathfrak{se}(3)$ are estimated for all views. 3D points are reconstructed through triangulation. Finally, the bundle adjustment jointly optimizes the 3D coordinates of the points $P := \{X_W^{(1)}, \dots, X_W^{(N)}\}$, camera poses $\Xi := \{\xi_1, \dots, \xi_M\}$ and intrinsic parameters of the pinhole model, remaining robust to noise. The first estimation is

based on COLMAP [36], using a minimal version to reduce computation time. During initialization, dimensions are defined at an arbitrary scale. Later, all data is scaled to metric using arbitrary scene constraints.

Plenoptic Bundle Adjustment. Plenoptic bundle adjustment begins with initial pinhole model values for intrinsic and extrinsic parameters and 3D object points, which are then refined using Levenberg-Marquardt optimization.

The main lens focal length f_L and principal point C_L are set during initialization using the pinhole model, while B and b_{L0} are determined via a linear least squares problem based on the relationship between the virtual depth v and the virtual image distance b_L (see Eq. (4)), set for every object point (see supplementary material for details). Distortion parameters are initialized to zero. Optimal parameters for the model in Sec. 3.1 are then refined by minimizing the cost function in Eq. (7) which can be adapted with any robust norm $\|\cdot\|_\gamma$.

$$E(\Pi, \Xi, P) = \sum_{i=1}^N \sum_{j=1}^M \sum_{k=1}^L \|r_{(i,j,k)}\|_\gamma \cdot \theta_{(i,j,k)} \quad (7)$$

In Eq. (7), Π includes intrinsic and distortion parameters, Ξ is the set of camera poses relative to a shared world frame ($\Xi := \{\xi_1, \dots, \xi_M\}$), P is the set of 3D reference points in the world frame ($P := \{X_W^{(1)}, \dots, X_W^{(N)}\}$). The object point $X_W \in P$ in the world frame, *e.g.* the frame of the first sequence view, can be converted to the camera frame of the j -th view by the rigid body transform $G(\xi_j) \in SE(3)$. The masking function $\theta_{(i,j,k)}$ is 1 if the i -th point of the object is visible in the k -th micro image of the j -th view, and is 0 otherwise. The residual vector $r_{(i,j,k)}$ for a point with measured coordinates X_{Rd} , corresponding to the point of object i seen in micro image k of camera view j , is defined by Eq. (8). The function $\pi_{ML}(\cdot)$ projects camera coordinates to the micro image k with the model defined in Sec. 3.1. This nonlinear optimization problem is solved using the Levenberg-Marquardt algorithm, implemented by the Ceres Solver Library [2].

$$r_{(i,j,k)} = \pi_{ML}\left(G(\xi_j)X_W^{(i)}, C_{ML}^{(k)}, \Pi\right) - X_{Rd}. \quad (8)$$

4 Evaluation

Several experiments were carried out to evaluate the performance of the proposed calibration pipeline, LiFCal, and to assess the quality of the resulting plenoptic camera model. Furthermore, to demonstrate the high quality and usability of the obtained plenoptic camera model, the model is applied in downstream tasks like metric depth estimation and SLAM. Here, we tightly integrate the plenoptic camera model into the depth estimation pipeline.

4.1 Calibration

Obtaining ground truth intrinsic parameters for any real camera model is almost impossible, and even more difficult for the complex model of a plenoptic

Table 1. Comparison of the intrinsic parameters of the plenoptic camera estimated by the reference method using a professional 3D calibration target and LiFCal. Deviations given in percentage are values relative to the respective reference calibration parameter.

Method	Lens	f_L [mm]	b_{L0} [mm]	B [mm]	c_x [pixel]	c_y [pixel]
Reference calibration (ground truth)	12.5 mm	13.181	12.209	0.399	1006.5	1041.5
	16 mm	16.748	15.893	0.376	1018.7	1054.2
	35 mm	35.368	34.471	0.370	1022.0	1031.0
LiFCal (our method)	12.5 mm	13.193	12.228	0.395	1006.5	1041.6
	16 mm	16.745	15.893	0.375	1019.4	1053.5
	35 mm	35.342	34.445	0.369	1024.0	1028.5
Deviation of	12.5 mm	0.091	0.155	1.003	0.000	0.010
LiFCal from the	16 mm	0.018	0.000	0.266	0.069	0.066
reference [%]	35 mm	0.074	0.075	0.270	0.196	0.242

camera. Therefore, we compare the results of LiFCal against a state-of-the-art calibration pipeline [42] that is utilizing a complex 3D calibration target and professional photogrammetric software to obtain high quality camera parameters. Several experiments were conducted to assess the repeatability and accuracy of the intrinsic camera parameters obtained by LiFCal.

Calibration Based on a 3D Calibration Target. In [42,49], the plenoptic camera is calibrated using a one-meter cube 3D target together with a professional photogrammetric measurement software. LiFCal is applied to the same calibration images for comparison with this state-of-the-art method. Sample images can be found in the supplementary material. [42] provides calibration data with a Raytrix R5 camera (model: MG042CG-CM-TG) with three different main lenses: $f_L = 12.5$ mm, $f_L = 16$ mm, and $f_L = 35$ mm. The camera has a resolution of 2048 pixels \times 2048 pixels and a pixel size of 5.5 μm . We use 94 images for the 12.5 mm lens, 70 images for the 16 mm lens, and 76 images for the 35 mm lens. The scene scale is obtained from known reference distances between markers on the target.

Tab. 1 compares the intrinsic camera parameters obtained by LiFCal with the reference calibration [42]. All parameters are estimated with relative errors below 0.3%, except for parameter B for the 12.5 mm lens (error of 1.003%), which can be explained by the small focal length compared to the object distance. The parameters’ accuracy is confirmed by the focal length f_L closely aligning with nominal manufacturer values. Also, the fixed manufacturing parameter B is consistent across estimates, with a small standard deviation of 0.013 mm. LiFCal achieves comparable results to [42] without using knowledge of the coded target markers, relying instead on standard SIFT features. While it struggles on homogeneous surfaces, it remains robust even with fewer features and images (see supplementary material for results with three different lenses).

Table 2. Estimated R5 camera parameters on target-free scenes and root mean square error (RMSE) relative to the reference. The RMSE compares acquired data with reference from Tab. 1. It is expressed as a percentage error relative to the reference because of significant differences in orders of magnitude among parameters (*e.g.*, nearly a factor of 50 between B and f_L) to interpret the error with respect to the parameter.

Scene	f_L [mm]	b_{L0} [mm]	B [mm]	c_x [pixel]	c_y [pixel]
Lab	16.609	15.889	0.338	1022.7	1056.9
Hallway	16.788	15.889	0.384	1019.3	1050.0
Office	16.771	15.881	0.379	1021.9	1045.8
RMSE [%]	0.505	0.048	5.981	0.292	0.535

Online Calibration on Target-free Scenes. To demonstrate the online calibration performance of LiFCal, we use sequences from a plenoptic VO dataset [49] captured with a Raytrix R5 camera (same as for previous experiment) with a nominal focal length of $f_L = 16$ mm. We take images at regular intervals of the winding movement at the start of three sequences: Lab (seq_004, using 56 images), Hallway (seq_007, using 70 images), Office (seq_009, using 76 images) (see supplementary material for samples). The scene scale is obtained from a real distance measured on a visible object in the images and applied as a scale factor to the scene.

The dataset contains sequences recorded only with the 16 mm lens, limiting evaluation in Tab. 2 to this configuration. However, the results can be compared with the 16 mm lines in Tab. 1. The RMSE relative to the reference across all three calibrations is well below 0.6% for all parameters, except B as before.

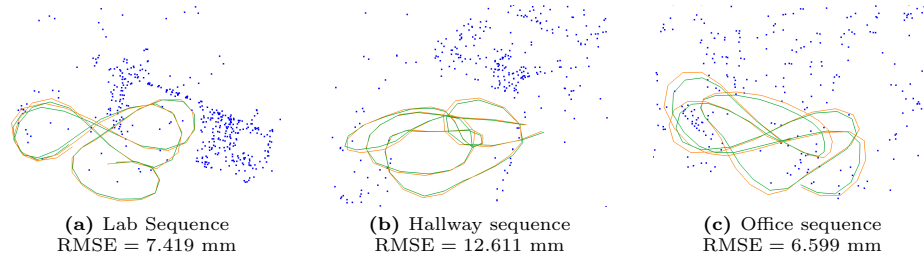
Online Recalibration. The plenoptic-camera-based online calibration still requires a reference scale in the scene to obtain metric model parameters. However, online calibration also allows the readjustment of model parameters *e.g.* obtained for a previous factory calibration. While some parameters may change and become inaccurate, others, such as the main lens focal length f_L and the distance B between the MLA and the sensor, remain fixed and are sensor and lens specific respectively. Therefore, in this experiment, we fix these parameters to reference values from [49], obviating additional steps for scene scale estimation. Pixel size becomes nonessential as parameters adapt accordingly, either in pixels or specified metric units. The sequences used are exactly the same as for the previous experiment.

Tab. 3 compares the optimized variable parameters and their reference values, demonstrating errors below 0.6% compared to the reference calibration. Here, no scene information is required, not even the scale. Nevertheless, the results are extremely close to the other experiments and to the reference.

Plenoptic Bundle Adjustment Accuracy. In all previous experiments, the camera model provided by LiFCal is compared to the reference calibration.

Table 3. Estimation of R5 camera parameters with recalibration by setting parameters $f_L = 16.748$ mm and $B = 0.376$ mm, and comparison with the reference in Tab. 1.

Scene	Estimated parameters			Deviation		
	b_{L0} [mm]	c_x [pixel]	c_y [pixel]	b_{L0} [%]	c_x [%]	c_y [%]
Lab	15.944	1014.6	1057.8	0.32	0.40	0.34
Hallway	15.869	1019.3	1051.6	0.15	0.06	0.25
Office	15.866	1024.4	1053.4	0.17	0.56	0.08

**Fig. 5.** Difference between the trajectories of the ground truth (*in orange*) and the camera poses estimated during calibration (*in green*) for the three sequences.

While the estimated parameters demonstrate high reproducibility, the experiments would not be able to disclose potential biases caused by the camera model. Therefore, we compare the camera poses obtained during the plenoptic bundle adjustment of the LiFCal calibration to the ground truth poses of [49] obtained with a synchronized stereo camera. Since the compared poses are obtained by two different sensors, potential model biases can be revealed. Fig. 5 shows the camera trajectory of the stereo reference from [49] and the one obtained by LiFCal, with the RMSE for each sequence. Positions are determined with centimeter-level precision for movements around 1 m in magnitude. The slightly higher error in the Hallway sequence can be attributed to the larger scale of the scene and the increased distance between objects and the camera.

Generalization to a Different Camera. Previous experiments were all performed with the same camera. To demonstrate the generalization of our pipeline to a different sensor, we also used a Raytrix R25 camera (model: R25-C-D-10G-A018-A), with a resolution of 5320 pixels \times 4600 pixels, a nominal focal length of $f_L = 12$ mm and a pixel size of 2.74 μm . Additional camera acquisitions introduce Aruco markers [17] printed on a sheet with known identifications and spacing. The markers are only used to define the scale of the scene directly. The acquired sequences are: Table (42 images), Phone (51 images), Keyboard (50 images). See supplementary material for reference.

Tab. 4 shows results from sequences with the same camera configuration. Estimated parameters are consistent across experiments, with a relative SD below 0.713% except for parameter B (SD of 11.519%) for the same reason as previ-

Table 4. Estimated R25 camera parameters on three scenes scaled with Aruco markers and their standard deviation (SD), to assess calibration repeatability across sequences. SD values are expressed as percentage error relative to the estimated mean parameter value for consistent analysis regardless of parameter magnitude.

Scene	f_L [mm]	b_{L0} [mm]	B [mm]	c_x [pixel]	c_y [pixel]
Table	13.163	11.893	0.386	2681.9	2272.0
Phone	13.062	11.927	0.330	2683.5	2297.5
Keyboard	12.977	11.929	0.310	2688.5	2295.4
SD [%]	0.713	0.170	11.519	0.128	0.619

ously noted. The absence of ground truth prevents defining the RMSE for the R25 camera.

4.2 Depth Estimation and SLAM

To showcase the usability and accuracy of the camera model obtained by LiFCal, we assess its effectiveness through various downstream tasks.

Metric Depth Estimation. Unlike other plenoptic camera models [18,43], LiFCal incorporates lens distortion directly into the raw image. This allows distortion to be corrected during the depth estimation and totally focused image synthesis. We extend an existing depth estimation pipeline [44,45] to directly generate undistorted metric depth maps and totally focused images (see Fig. 1) by using the camera model obtained by LiFCal. As shown in Fig. 6, the plenoptic camera model applied to the raw images prevents lens distortion from both the totally focused image (compare 6a and 6c) and the estimated depth (compare 6b and 6d). Also, as shown in Fig. 1, an estimated depth map can be projected to a metric 3D point cloud (more examples in the supplementary material).

Plenoptic-Camera-based SLAM. We calculate undistorted totally focused images and metric depth maps for sequences of [49]. Here, we project the virtual image space to a common image plane (using a central perspective projection explained in the supplementary material) to mimic an RGB-D sensor based on a pinhole camera model. Using this data, we run ORB-SLAM3 [5] in RGB-D mode without loop closure. Tab. 5 reports the trajectory error compared to reference poses and scale for the winding part of both indoors and outdoors scenes of [49]. The RMSE is below one centimeter for the Lab and Office scenes and slightly higher for Hallway and Parking due to larger displacements and distances. Notably, plenoptic camera depth data achieves accurate scene scaling, comparable to a dedicated plenoptic SLAM approach [48]. For example, Fig. 7 illustrates estimated trajectory for the Office sequence (seq. 9 of [49]), achieving an absolute scale error of 1.1%, a scale drift of 2.3%, a translational alignment error of 0.9% and a rotational error of 18.4° accumulated over the entire trajectory. Therefore,

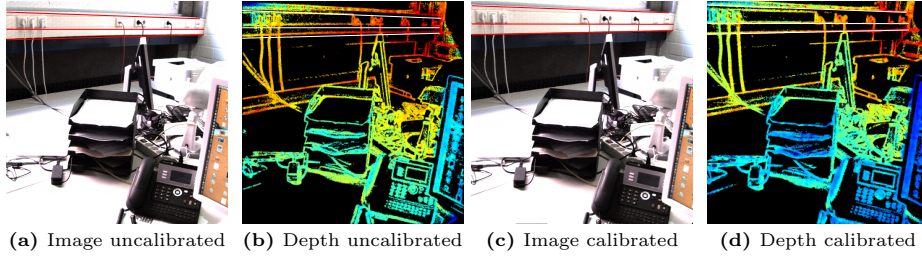


Fig. 6. Distortion correction in a totally focused image and a depth map: (a) and (b) show an uncalibrated image and its depth map with non-straight lines (respectively *red* and *white*); (c) and (d) show a calibrated image with its depth map of the same scene with straight lines.

Table 5. RMSE and scene scale calculated with ORB-SLAM3 and the calibrated plenoptic camera data against ground truth supplied by [49].

Metric	Lab	Hallway	Office	Parking
RMSE [mm]	9.775	78.993	6.060	46.636
Scale	0.980	0.847	0.999	1.057

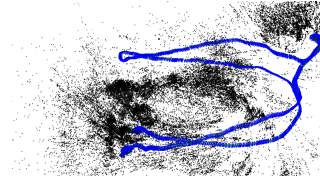


Fig. 7. SLAM with calibrated plenoptic data on the Office sequence of [49].

except for the rotational error, results for this sequence are similar to the ones of [48], despite ORB-SLAM3 not being optimized for plenoptic camera data.

5 Conclusion

We introduce LiFCal, a new online calibration pipeline for MLA-based light field cameras. We demonstrate that LiFCal can determine accurate and repeatable calibration results on target-free scenes with sufficient camera motion and features. By fixing camera specific pre-calibrated parameters, LiFCal can obtain accurate metric parameters even without any prior knowledge about the scene scale. We integrated the plenoptic camera model into a depth estimation pipeline to obtain metric point clouds of the scene. Besides metric depth estimation, we demonstrate the usability of the obtained camera model by integrating the calculated depth maps and totally focused images into a state-of-the-art RGB-D SLAM system.

Acknowledgments. We would like to thank the company Raytrix for providing a light field camera, which enabled us to conduct the experiments with data obtained by ourselves.

References

1. Adelson, E.H., Wang, J.Y.: Single lens stereo with a plenoptic camera. *Transactions on Pattern Analysis and Machine Intelligence (TPAMI)* **14**(2), 99–106 (1992). <https://doi.org/10.1109/34.121783>
2. Agarwal, S., Mierle, K., Team, T.C.S.: Ceres solver (Oct 2023)
3. Bok, Y., Jeon, H.G., Kweon, I.S.: Geometric calibration of micro-lens-based light field cameras using line features. *Transactions on Pattern Analysis and Machine Intelligence (TPAMI)* **39**(2), 287–300 (2017). <https://doi.org/10.1109/tpami.2016.2541145>
4. Brown, D.: Decentering distortion of lenses. *Photogrammetric Engineering* **32**(3), 444–462 (1966)
5. Campos, C., Elvira, R., Rodríguez, J.J.G., Montiel, J.M., Tardós, J.D.: Orb-slam3: An accurate open-source library for visual, visual-inertial, and multimap slam. *Transactions on Robotics (T-RO)* **37**(6), 1874–1890 (2021). <https://doi.org/10.1109/tro.2021.3075644>
6. Caprile, B., Torre, V.: Using vanishing points for camera calibration. *International journal of computer vision (IJCV)* **4**(2), 127–139 (1990). <https://doi.org/10.1007/BF00127813>
7. Chang, D., Huang, S., Zhou, Y., Qin, X., Ding, R., Hu, M.: Target-free stereo camera-gnss/imu self-calibration based on iterative refinement. *Sensors Journal* **24**(3), 3722–3730 (2024). <https://doi.org/10.1109/jsen.2023.3343371>
8. Cho, D., Lee, M., Kim, S., Tai, Y.W.: Modeling the calibration pipeline of the lytro camera for high quality light-field image reconstruction. In: *International Conference on Computer Vision (ICCV)*. pp. 3280–3287. IEEE (2013). <https://doi.org/10.1109/iccv.2013.407>
9. Dansereau, D.G., Pizarro, O., Williams, S.B.: Decoding, calibration and rectification for lenselet-based plenoptic cameras. In: *Conference on Computer Vision and Pattern Recognition (CVPR)*. pp. 1027–1034. IEEE (2013). <https://doi.org/10.1109/cvpr.2013.137>
10. Darwish, W., Bolsee, Q., Munteanu, A.: Plenoptic camera calibration based on sub-aperture images. In: *International Conference on Image Processing (ICIP)*. pp. 3527–3531. IEEE (2019). <https://doi.org/10.1109/icip.2019.8803473>
11. Engel, J., Koltun, V., Cremers, D.: Direct sparse odometry. *Transactions on Pattern Analysis and Machine Intelligence (TPAMI)* **40**(3), 611–625 (2018). <https://doi.org/10.1109/TPAMI.2017.2658577>
12. Engel, J., Schöps, T., Cremers, D.: Lsd-slam: Large-scale direct monocular slam. In: *European Conference on Computer Vision (ECCV)*. pp. 834–849. Springer (2014). https://doi.org/10.1007/978-3-319-10605-2_54
13. Fachada, S., Bonatto, D., Losfeld, A., Lafruit, G., Teratani, M.: Pattern-free plenoptic 2.0 camera calibration. In: *International Workshop on Multimedia Signal Processing (MMSP)*. pp. 1–6. IEEE (2022). <https://doi.org/10.1109/mmisp55362.2022.9949312>
14. Fachada, S., Losfeld, A., Senoh, T., Lafruit, G., Teratani, M.: A calibration method for subaperture views of plenoptic 2.0 camera arrays. In: *International Workshop on Multimedia Signal Processing (MMSP)*. pp. 1–6. IEEE (2021). <https://doi.org/10.1109/mmisp53017.2021.9733556>
15. Fang, J., Vasiljevic, I., Guizilini, V., Ambrus, R., Shakhnarovich, G., Gaidon, A., Walter, M.R.: Self-supervised camera self-calibration from video. In: *International Conference on Robotics and Automation (ICRA)*. pp. 8468–8475. IEEE (2022). <https://doi.org/10.1109/icra46639.2022.9811784>

16. Fischler, M.A., Bolles, R.C.: Random sample consensus: A paradigm for model fitting with applications to image analysis and automated cartography. *Communications of the ACM* **24**(6), 381–395 (Jun 1981). <https://doi.org/10.1145/358669.358692>
17. Garrido-Jurado, S., Muñoz-Salinas, R., Madrid-Cuevas, F.J., Marín-Jiménez, M.J.: Automatic generation and detection of highly reliable fiducial markers under occlusion. *Pattern Recognition* **47**(6), 2280–2292 (2014). <https://doi.org/10.1016/j.patcog.2014.01.005>
18. Heinze, C., Spyropoulos, S., Hussmann, S., Perwaß, C.: Automated robust metric calibration algorithm for multifocus plenoptic cameras. *Transactions on Instrumentation and Measurement (TIM)* **65**(5), 1197–1205 (2016). <https://doi.org/10.1109/tim.2015.2507412>
19. Ives, F.E.: Parallax stereogram and process of making same (1903), uS Patent 725,567
20. Ji, Z., Zhang, C., Wang, Q.: Light field camera self-calibration and registration. In: *Optoelectronic Imaging and Multimedia Technology*. vol. 10020, pp. 56–65. SPIE (2016). <https://doi.org/10.1117/12.2246339>
21. Johannsen, O., Heinze, C., Goldluecke, B., Perwaß, C.: On the calibration of focused plenoptic cameras. In: *Time-of-Flight and Depth Imaging. Sensors, Algorithms, and Applications: Dagstuhl 2012 Seminar on Time-of-Flight Imaging and GCPR 2013 Workshop on Imaging New Modalities*. pp. 302–317. Springer (2013). https://doi.org/10.1007/978-3-642-44964-2_15
22. Labussière, M., Teulière, C., Bernardin, F., Ait-Aider, O.: Blur aware calibration of multi-focus plenoptic camera. In: *Conference on Computer Vision and Pattern Recognition (CVPR)*. pp. 2542–2551. IEEE (2020). <https://doi.org/10.1109/cvpr42600.2020.00262>
23. Labussière, M., Teulière, C., Bernardin, F., Ait-Aider, O.: Leveraging blur information for plenoptic camera calibration. *International journal of computer vision (IJCV)* **130**(7), 1655–1677 (2022). <https://doi.org/10.1007/s11263-022-01582-z>
24. Lippmann, G.: Epreuves reversibles donnant la sensation du relief. *Journal de Physique Théorique et Appliquée* **7**(1), 821–825 (1908). <https://doi.org/10.1051/jphys:019080070082100>
25. Lopez, M., Mari, R., Gargallo, P., Kuang, Y., Gonzalez-Jimenez, J., Haro, G.: Deep single image camera calibration with radial distortion. In: *Conference on Computer Vision and Pattern Recognition (CVPR)*. pp. 11809–11817. IEEE (2019). <https://doi.org/10.1109/cvpr.2019.01209>
26. Lumsdaine, A., Georgiev, T.: The focused plenoptic camera. In: *International Conference on Computational Photography (ICCP)*. pp. 1–8. IEEE (2009). <https://doi.org/10.1109/iccphot.2009.5559008>
27. Lumsdaine, A., Georgiev, T., et al.: Full resolution lightfield rendering. *Indiana University and Adobe Systems, Tech. Rep* **91**, 92 (2008)
28. Mur-Artal, R., Tardós, J.D.: Orb-slam2: An open-source slam system for monocular, stereo, and rgb-d cameras. *Transactions on Robotics (T-RO)* **33**(5), 1255–1262 (2017). <https://doi.org/10.1109/tro.2017.2705103>
29. Ng, R.: *Digital Light Field Photography*. Stanford University (2006)
30. Ng, R., Levoy, M., Brédif, M., Duval, G., Horowitz, M., Hanrahan, P.: *Light Field Photography with a Hand-held Plenoptic Camera*. Ph.D. thesis, Stanford University (2005)
31. O’Brien, S., Trunpf, J., Ila, V., Mahony, R.: Calibrating light-field cameras using plenoptic disc features. In: *International conference on 3D vision (3DV)*. pp. 286–294. IEEE (2018). <https://doi.org/10.1109/3dv.2018.00041>

32. Perwass, C., Wietzke, L.: Single lens 3d-camera with extended depth-of-field. In: Human Vision and Electronic Imaging (HVEI). vol. 8291, pp. 45–59. SPIE (2012). <https://doi.org/10.1117/12.909882>
33. Pollefeys, M., Van Gool, L.: A stratified approach to metric self-calibration. In: Conference on Computer Vision and Pattern Recognition (CVPR). pp. 407–412. IEEE (1997). <https://doi.org/10.1109/cvpr.1997.609357>
34. Quenzel, J., Rosu, R.A., Houben, S., Behnke, S.: Online depth calibration for rgb-d cameras using visual slam. In: International Conference on Intelligent Robots and Systems (IROS). pp. 2227–2234. IEEE (2017). <https://doi.org/10.1109/iros.2017.8206043>
35. Rehder, E., Kinzig, C., Bender, P., Lauer, M.: Online stereo camera calibration from scratch. In: Intelligent Vehicles Symposium (IV). pp. 1694–1699. IEEE (2017). <https://doi.org/10.1109/ivs.2017.7995952>
36. Schönberger, J.L., Frahm, J.M.: Structure-from-motion revisited. In: Conference on Computer Vision and Pattern Recognition (CVPR). pp. 4104–4113. IEEE (2016). <https://doi.org/10.1109/CVPR.2016.445>
37. Wang, R., Schworer, M., Cremers, D.: Stereo dso: Large-scale direct sparse visual odometry with stereo cameras. In: International Conference on Computer Vision (ICCV). pp. 3903–3911. IEEE (2017). <https://doi.org/10.1109/iccv.2017.421>
38. Wang, Y., Wang, L., Liang, Z., Yang, J., An, W., Guo, Y.: Occlusion-aware cost constructor for light field depth estimation. In: Conference on Computer Vision and Pattern Recognition (CVPR). pp. 19777–19786. IEEE (2022). <https://doi.org/10.1109/cvpr52688.2022.01919>
39. Xiao, Z., Liu, Y., Gao, R., Xiong, Z.: Cutmib: Boosting light field super-resolution via multi-view image blending. In: Conference on Computer Vision and Pattern Recognition (CVPR). pp. 1672–1682. IEEE (2023). <https://doi.org/10.1109/cvpr52729.2023.00167>
40. Zeisl, B., Pollefeys, M.: Structure-based auto-calibration of rgb-d sensors. In: International Conference on Robotics and Automation (ICRA). pp. 5076–5083. IEEE (2016). <https://doi.org/10.1109/icra.2016.7487713>
41. Zeller, N., Noury, C.A., Quint, F., Teulière, C., Stilla, U., Dhome, M.: Metric calibration of a focused plenoptic camera based on a 3d calibration target. ISPRS Annals of the Photogrammetry, Remote Sensing and Spatial Information Sciences (ISPRS Annals) **III–3**, 449–456 (2016). <https://doi.org/10.5194/isprsannals-iii-3-449-2016>
42. Zeller, N.: Direct Plenoptic Odometry – Robust Tracking and Mapping with a Light Field Camera. Ph.D. thesis, Technische Universität München (2018)
43. Zeller, N., Quint, F., Stilla, U.: Calibration and accuracy analysis of a focused plenoptic camera. ISPRS Annals of the Photogrammetry, Remote Sensing and Spatial Information Sciences (ISPRS Annals) **II–3**, 205–212 (2014). <https://doi.org/10.5194/isprsannals-ii-3-205-2014>
44. Zeller, N., Quint, F., Stilla, U.: Establishing a probabilistic depth map from focused plenoptic cameras. In: International Conference on 3D Vision (3DV). pp. 91–99. IEEE (2015). <https://doi.org/10.1109/3dv.2015.18>
45. Zeller, N., Quint, F., Stilla, U.: Filtering probabilistic depth maps received from a focused plenoptic camera. BW-CAR Symposium on Information and Communication Systems (SInCom) **2**, 7–12 (2015)
46. Zeller, N., Quint, F., Stilla, U.: Depth estimation and camera calibration of a focused plenoptic camera for visual odometry. ISPRS Journal of Photogrammetry and Remote Sensing (P&RS) **118**, 83–100 (2016). <https://doi.org/10.1016/j.isprsjprs.2016.04.010>

47. Zeller, N., Quint, F., Stilla, U.: From the calibration of a light-field camera to direct plenoptic odometry. *Journal of Selected Topics in Signal Processing* **11**(7), 1004–1019 (2017). <https://doi.org/10.1109/jstsp.2017.2737965>
48. Zeller, N., Quint, F., Stilla, U.: Scale-awareness of light field camera based visual odometry. In: *European Conference on Computer Vision (ECCV)*. p. 732–747. Springer (2018). https://doi.org/10.1007/978-3-030-01237-3_44
49. Zeller, N., Quint, F., Stilla, U.: A synchronized stereo and plenoptic visual odometry dataset. *arXiv preprint* (2018). <https://doi.org/10.48550/arXiv.1807.09372>
50. Zhao, Y., Li, H., Mei, D., Shi, S.: Metric calibration of unfocused plenoptic cameras for three-dimensional shape measurement. *Optical Engineering* **59**(7), 073104–073104 (2020). <https://doi.org/10.1117/1.oe.59.7.073104>
51. Zhou, P., Cai, W., Yu, Y., Zhang, Y., Zhou, G.: A two-step calibration method of lenslet-based light field cameras. *Optics and Lasers in Engineering* **115**, 190–196 (2019). <https://doi.org/10.1016/j.optlaseng.2018.11.024>

LiFCal: Online Light Field Camera Calibration via Bundle Adjustment Supplementary Material

Aymeric Fleith^{1,2}, Doaa Ahmed², Daniel Cremers¹, and Niclas Zeller²

¹ Technical University of Munich, Munich, Germany
{aymeric.fleith, cremers}@tum.de

² Karlsruhe University of Applied Sciences, Karlsruhe, Germany
{doaa.ahmed, niclas.zeller}@h-ka.de

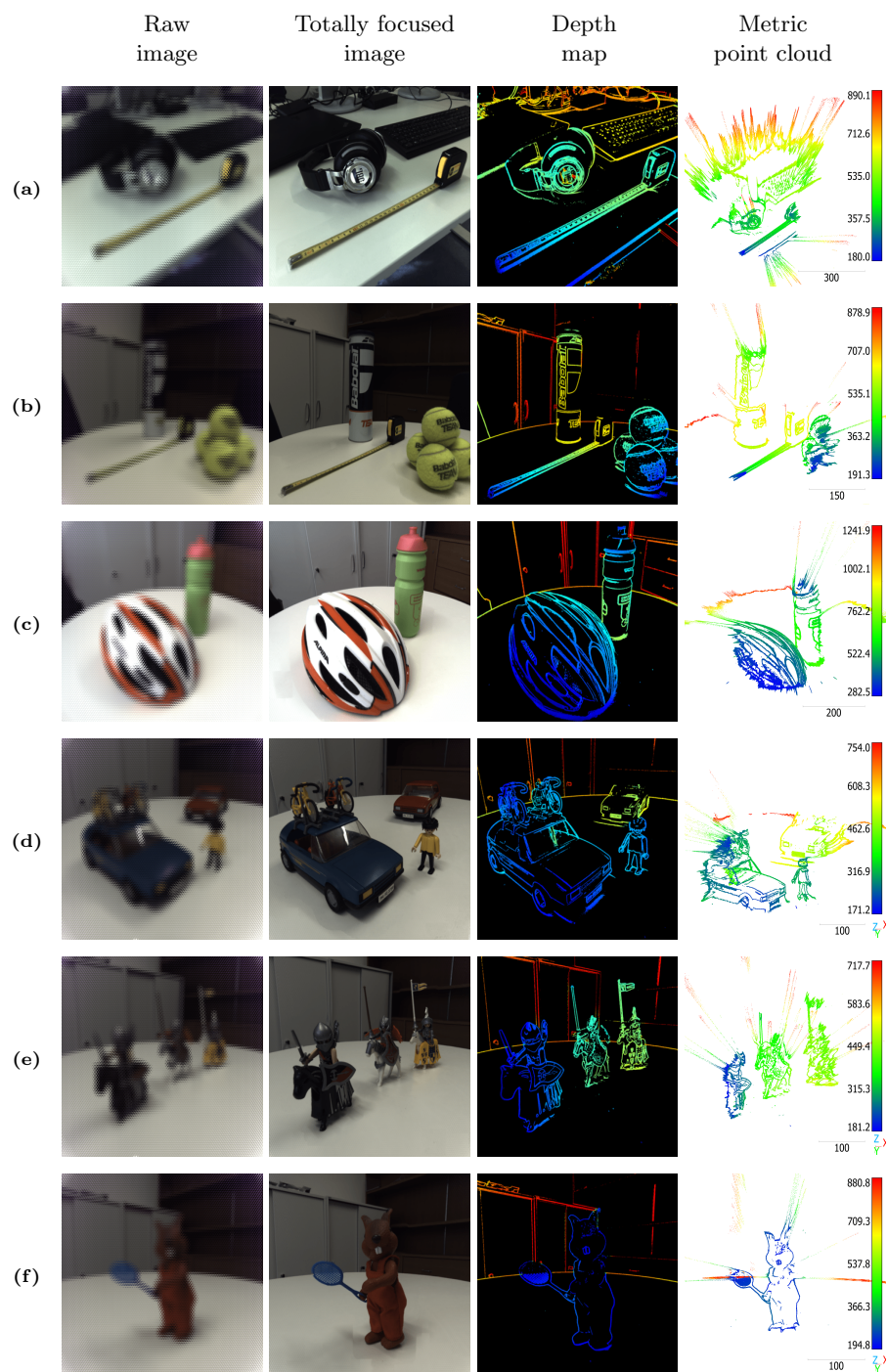
A Introduction

This supplementary material provides additional details and results beyond those in the main paper. Specifically, this includes the results of metric point clouds obtained using LiFCal calibration (Sec. B), the calculation of RGB-D data used for a SLAM task to mimic the data of a pinhole model (Sec. C), a detailed definition of the implemented distortion model (Sec. D), additional details regarding the initialization of the plenoptic camera model to perform bundle adjustment (Sec. E), sample images of the sequences used for the calibration experiments (Sec. F).

B Metric depth map results

To demonstrate the usability and accuracy of the LiFCal calibration method, we present results on several downstream tasks (see Sec. 4.2 in the main paper). This section presents examples of metric point clouds obtained by applying LiFCal calibration to raw data from several scenes.

Fig. 1 shows the resulting metric point clouds. For each scene, the following images are provided: raw image from the plenoptic camera, totally focused image corrected by the camera model obtained by LiFCal, depth map corrected by the camera model obtained by LiFCal, metric point cloud. Two calibration processes evaluated in the experiments were used in order to demonstrate performance of both. For the scenes in Fig. 1a, Fig. 1b, Fig. 1c, calibration is performed using the scene from Fig. 1a. The calculated model is retained for the sequences in Fig. 1b and Fig. 1c. For the other sequences in Fig. 1, camera calibration is performed with markers and kept fixed for sequences in Fig. 1d, Fig. 1e, Fig. 1f, Fig. 1g, Fig. 1h, Fig. 1i. In the right-hand column, the point cloud is completed with a distance scale and a depth scale, both expressed in millimeters.



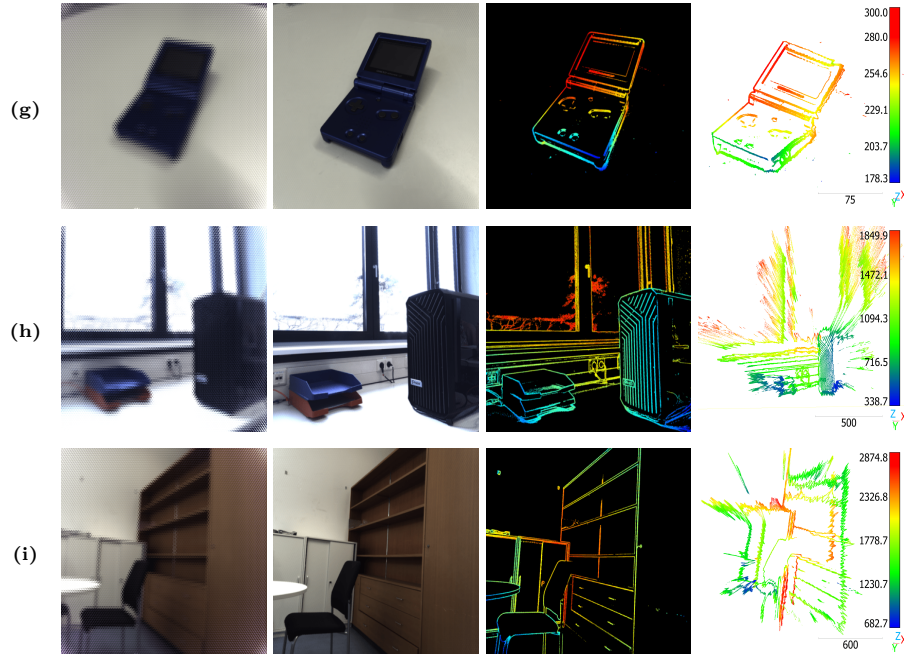


Fig. 1. Depth map results for several scenes. The point clouds in (a), (b), (c) are generated with a calibration on the scene (a). The point clouds in (d), (e), (f), (g), (h), (i) are generated with a calibration based on markers. In order, the different columns show: the raw image from the plenoptic camera, the totally focused image corrected by the LiFCal calibration, the depth map corrected by the LiFCal calibration and the metric point cloud of the scene. The point clouds are accompanied by a distance scale (*bottom right of each point cloud*) and a depth scale (*right of each point cloud*). Distance and depth data in the point clouds are in millimeters.

C RGB-D data calculation to run ORB-SLAM

We demonstrate the effectiveness of LiFCal calibration by integrating it into a SLAM task using the plenoptic camera (see Sec. 4.2 in the main paper). For this, we use ORB-SLAM3 [5] in its version with RGB-D data, disabling loop closure.

ORB-SLAM3 uses a pinhole camera model. To mimic this model with the plenoptic camera, we perform a central perspective projection as shown in Fig. 2. Each point X'_V in virtual space is formed at a different distance from the MLA, depending on its distance from the camera. Instead of projecting the points horizontally (as shown in orange), they are projected onto the projection plane along a straight line passing through the center of the main lens (illustrated projection in blue). In principle, the projection plane can be set at an arbitrary distance from the MLA. We choose a distance between the MLA and the projection plane of $2B$ corresponding to the total covering plane defined in [32]. It corresponds to a virtual depth of $v = 2$, which is the furthest distance from the camera for which

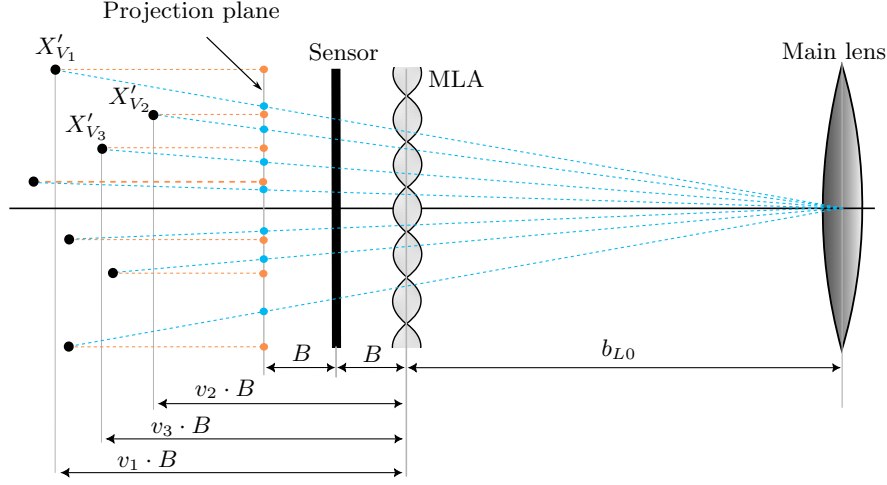


Fig. 2. Central perspective projection of the virtual image to a common image plane to mimic a pinhole camera model to use the data with ORB-SLAM. The points of the virtual image are projected along a straight line passing through the center of the main lens (*blue*) instead of horizontally (*orange*). The distance between the MLA and the projection plane is chosen at $2B$.

a depth can be measured. This projection ensures that the edges of the image are not too large. Projection is performed using similar triangles. The coordinates of the new point $X_{proj} = [x_{proj}, y_{proj}]^T$ after projection of $X'_V = [x'_V, y'_V, z'_V = v]^T$ are calculated using Eq. (1) and Eq. (2).

$$x_{proj} = \frac{x'_V - c_x}{v \cdot B + b_{L0}} \cdot (2 \cdot B + b_{L0}) + c_x \quad (1)$$

$$y_{proj} = \frac{y'_V - c_y}{v \cdot B + b_{L0}} \cdot (2 \cdot B + b_{L0}) + c_y \quad (2)$$

In Eq. (1) and Eq. (2), v is the virtual depth of the point, B is the distance between MLA and sensor, b_{L0} is the distance between main lens and MLA and $C_L = [c_x, c_y]^T$ is the principal point of the main lens.

ORB-SLAM3 requires metric depth data. The metric depth is then determined by the thin lens equation using Eq. (3). The parameter f_L is the focal length of the main lens, b_L is the distance between the main lens and the virtual image and z_C is the distance between the real object and the main lens.

$$z_C = \left(\frac{1}{f_L} - \frac{1}{b_L} \right)^{-1} \quad \text{with} \quad b_L = b + b_{L0} \quad \text{and} \quad b = v \cdot B \quad (3)$$

D Distortion Model

As described in the main paper (see Sec. 3.1), lens distortion is defined directly on raw image coordinates $X_R = [x_R, y_R]^T$. Using this model, we implicitly account for both main lens distortion, and sensor and MLA misalignment. The model uses radial symmetric distortion and tangential distortion according to the model presented in [4]. Nevertheless, it can be replaced by any other distortion model. Distortion is applied both to the raw image points on the sensor and to the centers of the micro images or micro lenses respectively. For the sake of notation, we define x'_R and y'_R as follows:

$$x'_R = x_R - c_x, \quad y'_R = y_R - c_y. \quad (4)$$

The radial symmetric distortion is characterized by a polynomial with respect to the radius r given in Eq. (5) where k_n is the $(n+1)$ -th coefficient. The radius r is defined as the Euclidean distance between a point X_R and the main lens principal point.

$$\Delta r_{rad} = \sum_{n=0}^{\infty} k_n r^{2n+3} \quad \text{with} \quad r = \sqrt{x'^2_R + y'^2_R} \quad (5)$$

Trigonometrically projecting Eq. (5) onto the two axes gives the Δx_{rad} and Δy_{rad} correction terms in the image's Cartesian coordinate system. Retaining only the first three coefficients results in Eq. (6) and Eq. (7) respectively.

$$\Delta x_{rad} = x'_R \frac{\Delta r_{rad}}{r} = x'_R \cdot (k_0 r^2 + k_1 r^4 + k_2 r^6) \quad (6)$$

$$\Delta y_{rad} = y'_R \frac{\Delta r_{rad}}{r} = y'_R \cdot (k_0 r^2 + k_1 r^4 + k_2 r^6) \quad (7)$$

The tangential distortion is defined with the first two parameters p_0 and p_1 . The expressions in both directions are given in Eq. (8) and Eq. (9) respectively.

$$\Delta x_{tan} = p_0 \cdot (r^2 + 2x'^2_R) + 2p_1 x'_R y'_R \quad (8)$$

$$\Delta y_{tan} = p_1 \cdot (r^2 + 2y'^2_R) + 2p_0 x'_R y'_R \quad (9)$$

The radial and tangential corrections can be combined to obtain the coordinates of the distorted point $X_{Rd} = [x_{Rd}, y_{Rd}]^T$ from the base x_R and y_R coordinates:

$$x_{Rd} = x_R + \Delta x_{rad} + \Delta x_{tan}, \quad (10)$$

$$y_{Rd} = y_R + \Delta y_{rad} + \Delta y_{tan}. \quad (11)$$

Since the distortion model defined in Eq. (8) and Eq. (9) affects all raw image coordinates on the sensor, the same distortion model is implicitly applied to the micro image centers $C_I = [c_{Ix}, c_{Iy}]^T$ as well.

To project an object point onto the image sensor (*e.g.* during plenoptic bundle adjustment), the distortion model can be applied in the forward direction

as defined in Eq. (10) and Eq. (11). However, for downstream tasks like depth estimation, the distortion model needs to be inverted. Because the defined polynomials are not directly invertible, this, in general, is done in an iterative manner. Nevertheless, this undistortion process can be calculated beforehand and can be applied directly to the entire recorded raw image. Defining the distortion on raw image coordinates has the advantage that after undistorting the raw image, tasks like depth estimation, image synthesis, etc. can be carried out without considering the distortion anymore.

E Initialization of plenoptic camera parameters

As described in the main paper (Sec. 3.2), after the initialization phase, the parameters of the plenoptic camera model need to be initialized. The main lens focal length f_L and the principal point C_L can be set during the initialization using the pinhole model. The additional plenoptic parameters B and b_{L0} are initialized by solving the linear Eq. (12) obtained from the plenoptic camera model. This equation is set up for each feature point observed in a calibration image.

$$b_L = v \cdot B + b_{L0} \quad (12)$$

Here, v is the virtual depth which can be estimated based on the recorded raw image [44] and b_L is the corresponding main lens image distance which is obtained from the thin lens equation defined in Eq. (13).

$$b_L = \left(\frac{1}{f_L} - \frac{1}{z_C} \right)^{-1} \quad (13)$$

In Eq. (13), z_C is the object distance *i.e.* the third component of the camera coordinates $X_C = [x_C, y_C, z_C]^T$ of the corresponding object points. For each point, X_C is calculated using the estimation object point coordinates $X_W = [x_W, y_W, z_W]^T$ and the corresponding camera pose $\Xi \in \text{SE}(3)$ obtained during initialization (see Sec. 3.2 in the main paper).

Using the estimated virtual depths v_i and calculated image distances b_{Li} ($i \in \{1, \dots, N\}$) for N points, the following linear system of equations can be defined (Eq. (14)).

$$\begin{bmatrix} b_{L1} \\ b_{L2} \\ \vdots \\ b_{LN} \end{bmatrix} = \begin{bmatrix} v_1 & 1 \\ v_2 & 1 \\ \vdots & \vdots \\ v_N & 1 \end{bmatrix} \cdot \begin{bmatrix} B \\ b_{L0} \end{bmatrix}$$

$$B_L = V \cdot \begin{bmatrix} B \\ b_{L0} \end{bmatrix} \quad (14)$$

Initialization for the parameters B and b_{L0} is obtained as a standard least-squares solution defined as follows:

$$\begin{aligned} \begin{bmatrix} B \\ b_{L0} \end{bmatrix} &= (V^T \cdot V)^{-1} \cdot V^T \cdot B_L, \\ \begin{bmatrix} B \\ b_{L0} \end{bmatrix} &= \left(\begin{bmatrix} v_1 & v_2 & \cdots & v_N \\ 1 & 1 & \cdots & 1 \end{bmatrix} \cdot \begin{bmatrix} v_1 & 1 \\ v_2 & 1 \\ \vdots & \vdots \\ v_N & 1 \end{bmatrix} \right)^{-1} \cdot \begin{bmatrix} v_1 & v_2 & \cdots & v_N \\ 1 & 1 & \cdots & 1 \end{bmatrix} \cdot \begin{bmatrix} b_{L1} \\ b_{L2} \\ \vdots \\ b_{LN} \end{bmatrix}. \end{aligned} \quad (15)$$

F Sequences for calibration experiments

In this section, we show exemplary extracts from the totally focused images of the sequences used in each experiment provided in the evaluation section of the main paper (Sec. 4). Tab. 1 summarizes the sequences used for each experiment.

Table 1. Association of image sequence extracts used in each calibration evaluation experiment with our LiFCal method.

Experiment	Sequences used
Calibration based on a 3D calibration target	Fig. 3
Online calibration on target-free scenes	Fig. 4
Online recalibration	Fig. 4
Generalization to a different camera	Fig. 5

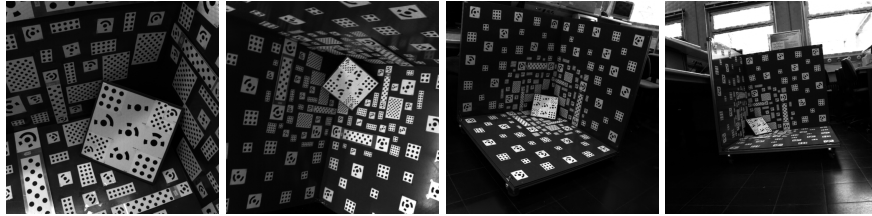


Fig. 3. Images of the sequence with the 3D target used in [42]. 94 images for the 12.5 mm lens, 70 images for the 16 mm lens and 76 images for the 35 mm lens.



Fig. 4. Sample of the totally focused images of the sequence for online calibration: (a) Lab (56 images from seq_004), (b) Hallway (70 images from seq_007), (c) Office (76 images from seq_009).



Fig. 5. Sample of the totally focused images of the sequence for calibration on any scene using Aruco markers for scaling: (a) Table (42 images), (b) Phone (51 images), (c) Keyboard (50 images).

G Reducing the number of features in the scene

To demonstrate the robustness of the calibration pipeline even with fewer features, it was applied by varying the number of points and the number of images used. The data used are those with the calibration target (see example images in Fig. 3), so that the RMSE can be calculated in relation to the reference given in [42]. The experiment was carried out with three different lenses mounted on the R5 camera: $f_L = 12.5$ mm (Fig. 6), $f_L = 16$ mm (Fig. 7), and $f_L = 35$ mm (Fig. 8).

With sufficient images and points, our LiFCal method achieves an RMSE of around 0.5% compared with the ground truth. Errors are slightly higher for the 35 mm lens, which can be explained by the inferior scattering of points in the image due to the higher focal length. The data starts to become a little less precise with less than 800 points and fewer than 25 images. Nevertheless, correct calibration data are still obtained down to 75 points and 15 images.

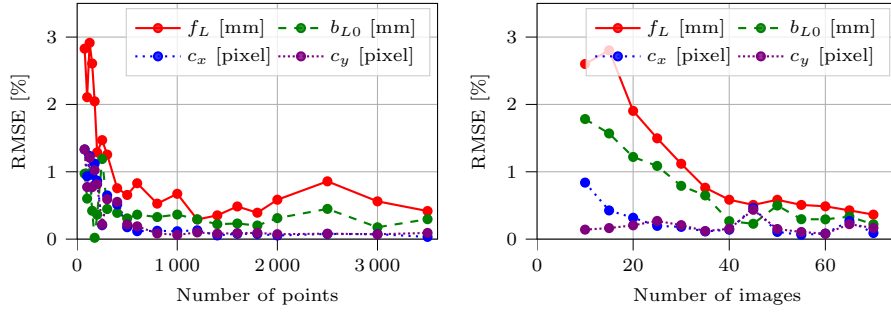


Fig. 6. RMSE over 10 runs (in percentage of the ground truth) relative to the number of points (with 30 images) (*left*) and relative to the number of images (with 1500 points) (*right*) used for bundle adjustment with the 12.5 mm lens.

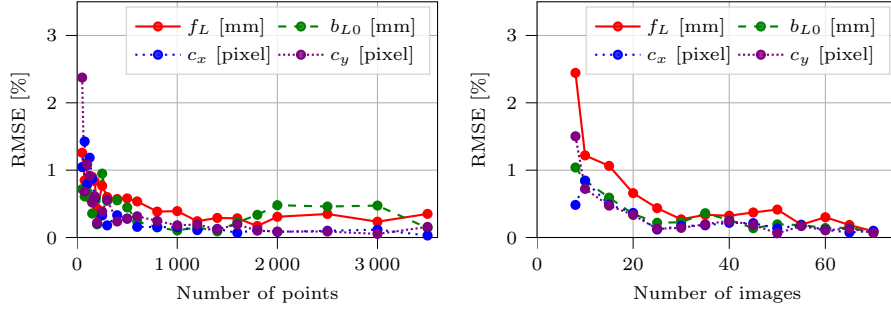


Fig. 7. RMSE over 10 runs (in percentage of the ground truth) relative to the number of points (with 30 images) (*left*) and relative to the number of images (with 1500 points) (*right*) used for bundle adjustment with the 16 mm lens.

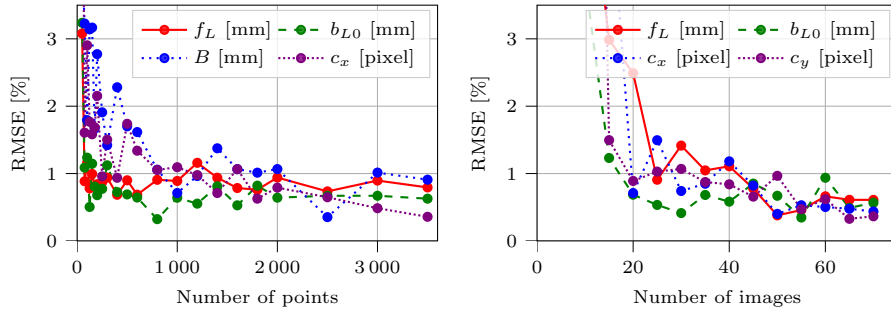


Fig. 8. RMSE over 10 runs (in percentage of the ground truth) relative to the number of points (with 30 images) (*left*) and relative to the number of images (with 1500 points) (*right*) used for bundle adjustment with the 35 mm lens.